

Phase Behavior and Kinetics of Phase Separation of a Nonionic Microemulsion of C₁₂E₅/Water/1-Chlorotetradecane upon a Temperature Quench

G. Roshan Deen,* Cristiano L. P. Oliveira, and Jan Skov Pedersen

Soft Matter Group, Department of Chemistry and Nano science Center (i-NANO), University of Aarhus, Langelandsgade 140, Aarhus C, Denmark

Received: September 17, 2008; Revised Manuscript Received: March 3, 2009

The phase behavior and phase separation kinetics of a model ternary nonionic microemulsion system composed of pentaethylene glycol dodecyl ether (C₁₂E₅), water, and 1-chlorotetradecane were studied. With increasing temperature, the microemulsion exhibits the following rich phase behavior: oil-in-water phase (L₁+O), droplet microemulsion phase (L₁), lamellar liquid crystalline phase (L_∞), and sponge-like (liquid) phase (L₃). The microemulsion with a fixed surfactant-to-oil volume fraction ratio (Φ_s/Φ_o) of 0.81 and droplet volume fraction of 0.087 was perturbed from equilibrium by a temperature quench from the L₁ region (24 °C) to an unstable region L₁+O (13 °C), where the excess oil phase is in equilibrium with the microemulsion droplets. The process of phase separation in the unstable region was followed by time-resolved small-angle X-ray scattering (TR-SAXS) and time-resolved turbidity methods. Due to the large range of scattering vector ($q = 0.004\text{--}0.22\text{ \AA}^{-1}$) that is possible to access with the TR-SAXS method, the growth of the oil droplets and shrinking of the microemulsion droplets as a result of phase separation could be studied simultaneously. By using an advanced polydisperse ellipsoidal hard-sphere model, the experimental curves have been quantitatively analyzed. The microemulsion droplets were modeled as polydisperse core-shell ellipsoidal particles, using molecular constraints, and the oil droplets are modeled as polydisperse spheres. The radius of gyration (R_g) of the growing oil droplets, volume fraction of oil in the microemulsion droplets, and polydispersity were obtained from the fit parameters. The volume equivalent radius at the neutral plane between the surfactant head and tail of the microemulsion droplet decreased from 76 to 51 Å, while the radius of oil drop increased to 217 Å within the 160 min of the experiment. After about 48 min from the temperature quench, the system reaches a steady state and continues to coarsen at a constant fraction of the oil of 0.51 in the oil phase by Ostwald ripening with the power law dependence of $R_{oil} \propto t^{1/3}$. The size of the oil droplets determined by the time-resolved turbidity method is in good agreement with that of the TR-SAXS, highlighting the usefulness of the method in the size determination of oil-in-water microemulsions on an absolute scale.

Introduction

Microemulsions are thermodynamically stable multicomponent systems consisting of oil, water, and a surfactant.^{1–3} On a microscopic level, the surfactant molecules separate the oil and water into two subphases by adsorbing at the interface as an interfacial film. Depending on the nature of the surfactant, temperature, composition, etc., various phases of microemulsions such as droplet, lamellar, bicontinuous, networks, etc., are formed.^{4,5} The characteristic length scales of such microstructures vary between 1 and 100 nm. Since the preparation of the first microemulsion in 1940s, these systems⁶ have been increasingly studied due to their potential applications in oil recovery, catalytic reactions, synthesis of nanoparticles, preconcentrated drug formulations, polymerization media, etc.^{7–10}

Interest in nonionic microemulsions containing alkyl poly(ethylene glycol) ether surfactants (C_{*i*}E_{*j*}) and *n*-alkanes has increased owing to the rich phase behavior of such surfactants as a function of temperature.¹¹ By varying the temperature, the spontaneous curvature of the surfactant film can be varied, leading to the formation of various phases. This is due to the strong temperature-dependent interactions of water and ethylene

oxide groups of the surfactant.^{12–14} Water changes from a good solvent to a bad solvent with increasing temperature. At lower temperatures, the ethylene oxide group prefers to swell to high water content, resulting in a preferred curvature toward oil. At higher temperatures, the ethylene oxide groups prefers lower water content due to the disruption of hydrogen bonds and the film tends to curve toward water. This curvature property of the surfactant film can quantitatively be described¹¹ in terms of spontaneous mean curvature H_0 . By definition, $H_0 = 0$ at the phase inversion temperature T_0 , where the surfactant film does have a preferred curvature either toward oil or water and can be written as

$$H_0(T) = c(T_0 - T) \quad (1)$$

where T_0 is the balance temperature of the microemulsion and c is the coefficient that is slightly dependent on the nature of the surfactant, which is approximately $10^{-3} (\text{K nm})^{-1}$ for C₁₂E₅ surfactant.^{15,16} It is this temperature-dependent property of C_{*i*}E_{*j*} type surfactants that forms the underlying basis for describing the equilibrium phase behavior of microemulsions and emulsification processes in particular.^{17,18} Therefore, starting from a microemulsion, an emulsion can be obtained by inducing a change in the spontaneous curvature by changing the temperature of the system.

On the basis of the work of Shinoda,¹⁹ the emulsification process can be described as a transition from a water-in-oil

* To whom correspondence should be addressed. Present address: Natural Science & Science Education, National Institute of Education, Nanyang Technological University, 1 Nanyang Walk, Singapore 637616. E-mail: roshan.gulam@nie.edu.sg.

(w/o) microemulsion to an oil-in-water microemulsion (o/w) via the bicontinuous or lamellar microemulsion. The final o/w microemulsion is also an equilibrium state where the microemulsion phase coexists with the excess oil that phase separates as the second phase. This state is normally denoted as the L₁+O phase. This type of emulsification process^{20,21} is exploited for producing monodisperse latex particles,²² gel emulsions,^{23,24} etc.

In the L₁+O phase, the microemulsion droplets may exchange material, viz., the oil, by a number of different processes^{17,25–27} such as (i) coalescence of small droplets into a large droplet, (ii) micelle mediated oil transfer between droplets, or (iii) diffusion of individual molecules through the continuous medium. Although all three mechanisms of material exchange have been observed for various systems, it has to be pointed out that this subject is still open for debate due to the nonemergence of a consistent picture. The reasons being that the above mechanisms greatly depend on a subtle balance of droplet interactions, nature of the surfactant, solubility of oil in the aqueous phase, nature of temperature quench, etc.^{17,18,27–29} Therefore, a detailed understanding of any new microemulsion system is a prerequisite to understanding its equilibrium and material exchange properties.

In this present article, we present the study of a nonionic model microemulsion system containing chlorinated oil, viz., C₁₂E₅/water/1-chlorotetradecane. Microemulsions containing chlorinated oils have gained importance due to their potential applications in reaction catalysis, enhanced oil recovery, product separation, etc.^{28–33} The detailed temperature-dependent phase behavior of the new system has been established.³⁴ Emulsification of the system is achieved by a temperature quench of the microemulsion phase (L₁) from 24 °C into the unstable (L₁+O) phase (13 °C). This results in perturbation of equilibrium, and the system phase separates with excess oil as the second phase as a result of changes in the spontaneous curvature of the surfactant film. The process of phase separation is followed by a time-resolved SAXS method in the high-resolution configuration, and the results are quantitatively analyzed using a polydisperse core–shell ellipsoidal model. The high-resolution configuration of the SAXS setup provides an extended range of scattering vector of $q = 0.004\text{--}0.22\text{ \AA}^{-1}$ which gives the possibility to study the dynamic changes of both small and large droplets in an emulsification process without the need for contrast matching of any of the components.²⁹ The scattering vector q is defined as

$$q = \frac{4\pi}{\lambda} \sin\left(\frac{\theta}{2}\right) \quad (2)$$

where λ is the wavelength of X-rays (1.542 Å Cu K α) and θ is the scattering angle.

Our approach to emulsification by a temperature quench and the proposed model to quantify the experimental results thus permit us to study both early and late stage kinetics of phase separation in microemulsions.

Experimental Section

Materials. All chemicals and reagents were used as received. High-grade pentaethylene glycol dodecylether (C₁₂E₅) (purity by GC > 98%) and 1-chlorotetradecane were obtained from Nikko Chemicals and Aldrich, respectively. Milli-Q water was used for all sample preparations.

Preparation of Microemulsions and Phase Behavior. Microemulsion samples of different droplet volume fractions were prepared by weight at room temperature. The surfactant-to-oil volume fraction ratio (Φ_s/Φ_o) which defines the constraint of

the area-to-the-enclosed-volume ratio and gives maximum curvature toward oil was fixed at 0.81. For this chosen value, spherical microemulsion droplets with maximum curvature toward oil and with low polydispersity were obtained. Appropriate amounts of C₁₂E₅, water, and 1-chlorotetradecane were accurately weighed and mixed thoroughly using a high-speed vortex mixer for complete homogenization. The samples were heated to 45 °C in an oven and air cooled to room temperature for complete solubilization of the components. The weight of the components of the microemulsion was then converted to volumes using their appropriate densities. The following values of densities (g/cm³) at room temperature were used: C₁₂E₅, 0.978; 1-chlorotetradecane, 0.859; water, 0.9980. The microemulsion droplet volume fraction was defined as

$$\Phi_{\text{droplet}} = \frac{V_s + V_o}{V_s + V_o + V_w} \quad (3)$$

where V_s , V_o , and V_w are the volume of surfactant, oil, and water, respectively.

The boundaries of each phase of the microemulsions were determined³⁵ both by visual observation and between crossed polarizers (“Titoscope” manufactured at the Center of Physical Chemistry, University of Lund, Sweden). The samples were placed in a thermostatted water bath (Ika labortechnik), and the temperature was increased in steps of 1 °C from 20 to 80 °C and the visual changes were recorded. The phase boundary of the lamellar phase is where the samples lost their birefringence. The exact clear–turbid boundaries for the characterization of the droplet L₁ phase were determined by measuring the change in turbidity as a function of temperature in a UV–vis spectrophotometer at a wavelength of 488 nm (Perkin-Elmer Lambda 25, equipped with a Perkin-Elmer PTP1 Peltier temperature control). After the visual observation experiments, the samples were rehomogenized by heating them up to the L _{α} phase and cooling to room temperature. The phase behavior procedure was then repeated to confirm the observations.

Density Measurements. The density of 1-chlorotetradecane and water at the temperature of interest (24 and 13 °C) was measured on a DMA 5000 densitometer (Anton-Paar, Graz) which uses the oscillating-tube technique. The instrument was calibrated at 20 °C using air and water as references prior to measurements of the samples. Approximately 1.5 mL of the sample was required for each measurement and the measurement was repeated at least three times on the same day until reproducible results were obtained. The electron density of C₁₂E₅, water, and 1-chlorotetradecane was calculated using their appropriate molar volumes.^{36,37}

Time-Resolved High-Resolution Small-Angle X-ray Scattering (SAXS). The measurements were performed on the modified NanoSTAR SAXS at the University of Aarhus.³⁸ The instrument is a modified version of commercially available SAXS equipment (Bruker AXS). It is optimized with respect to flux and background and therefore ideally suited for solution scattering. The instrument uses a rotating anode X-ray source and is equipped with multilayer parabolic Göbel mirrors. The configuration of the instrument in the high-resolution configuration provides a range of scattering vector moduli q from 0.004 to 0.22 Å^{−1} with a flux of 10⁶ photons per second. The sample-to-detector distance was 106.70 cm. The high-resolution version uses small pinholes (0.5 mm Ø of source pinhole, 0.15 mm Ø of defining pinhole, and 0.5 mm Ø of the antiscatter pinhole in front of the sample) and a small beamstop (2.0 mm Ø). It can thus reach smaller values of the scattering vector.²⁷

The samples are held in home-built quartz capillary holders sealed with steel caps and o-rings. The capillary is placed in a thermostatted sample block for good thermal contact. For temperature driven kinetics measurements, the temperature of the samples was quenched from 24 to 13 °C using a Peltier temperature controller (Anton-Paar), and scans were collected for various time intervals such as 2, 3, 5, 10, 15, and 30 min. The quench from 24 to 13 °C was relatively fast (~30 s), while it took 2 min for the sample to reach the quench temperature. The exact time that it took for the sample to attain the desired temperature was prior established by measuring the temperature of the sample using a platinum resistance thermometer.

Time-Resolved Turbidity Measurements. The turbidity of the microemulsion of droplet volume fraction 0.087 and fixed Φ_s/Φ_o ratio of 0.81 was measured in a Perkin-Elmer Lambda 25 UV-vis spectrophotometer which was connected to a temperature controller (Perkin-Elmer PTP-1 Peltier element). Samples were quenched from 24 to 13 °C, and the change in turbidity was recorded at a wavelength of $\lambda = 588$ nm as a function of time. The quench from 24 to 13 °C was fast (~60 s), while it took 3 min for the sample to reach the quench temperature.

As the measured turbidity is defined as $\log(I_0/I_t)$ where I_0 and I_t are the incident and transmitted light intensities, respectively, the path length normalized turbidity (τ) is then related to the sample turbidity measured at a fixed wavelength at which there is no molecular absorption as³⁹

$$I_t = I_0 \exp(-\tau l) \quad (4)$$

$$\tau = \frac{2.303 \times \log(I_0/I_t)}{l} \quad (5)$$

where l is the path length of light in the cuvette (1 cm).

Hard-Sphere Polydisperse Model. To quantitatively analyze the SAXS spectra on the absolute scale, a polydisperse core-shell model composed of ellipsoids of revolution with hard-sphere interactions was used for modeling the microemulsion droplets.⁴⁰ Formally, the intensity can be written as a product of a form factor and a structure factor

$$I(q) = \int_0^\infty n(R) \langle F(q, R)^2 \rangle dR + \frac{1}{N} \int_0^\infty \int_0^\infty n(R) n(R') \langle F(q, R) \rangle \langle F(q, R') \rangle [S(q, R, R') - 1] dR dR' \quad (6)$$

where $n(R)$ is the number size distribution, N is the total number of particles, and $S(q, R, R')$ are partial structure factors between spheres of radii R and R' :

$$\langle F(q, R)^n \rangle = \int_0^{\pi/2} F(q, R, \varepsilon, \theta)^n \sin \theta d\theta \quad (7)$$

is the orientation averaged particle form factor. The particles were taken as core-shell ellipsoids of revolution with dimensions $(R, R', \varepsilon R)$, and molecular constraints⁴¹ were used to scale the amount of surfactant in the droplets with surface area at the neutral plane between the polar headgroup and the apolar tails of the surfactant. The particles consisted of a core and two shells, one for the hydrocarbon tails and the headgroup of the surfactant, respectively. The scattering length density of each component was calculated from the known partial specific densities, and water penetration in the surfactant headgroup region was allowed.

The excess oil droplets were described as polydisperse spheres, and any concentration effects on the scattering from these were neglected:

$$I_{\text{oil}}(q) = \int_0^\infty n_{\text{oil}}(R) F_{\text{oil}}(q, R)^2 dR \quad (8)$$

where $n_{\text{oil}}(R)$ and $F_{\text{oil}}(q, R)^2$ are the number size distribution and form factor of the oil droplets, respectively. The scattering length density of the oil droplets was taken as that of the pure oil. The partitioning of the oil in the microemulsion droplets and in the pure oil droplet was described by a fit parameter, with the amount of oil being conserved. The size of the microemulsion droplets, oil droplets, and relative polydispersity values were obtained from the fits. The radius of gyration (R_g) for the oil droplets was calculated from the size distribution. The terms entering eqs 6–8 are very involved for the full expressions and therefore are not given in the paper, but they can be found in the original work of Vrij.^{42,43}

Results and Discussion

Phase Behavior of Microemulsion. The “fish”-cut phase diagram for the nonmicroemulsion reported in this work has been described in detail in our earlier report.³⁴ The partial phase diagram of the microemulsion containing various droplet volume fractions and a fixed Φ_s/Φ_o ratio of 0.81 is shown in Figure 1. This ratio indicates a water-rich oil-in-water microemulsion phase. With an increase in temperature, the formation of various phases can be observed. The clear microemulsion droplet phase lies in the temperature range 18–25 °C, and below the lower boundary, it is in equilibrium with pure oil ($L_1 + O$). In the temperature region between 25 and 30 °C (marked with a dotted line), the clear microemulsion becomes light bluish and shows no optical birefringence. This bluish region could possibly be due to the formation of large cylindrical structures that can scatter light.^{33,34} Above this region, the surfactant molecules organize into a lamellar bilayer (L_α) phase exhibiting optical birefringence. Further, above the lamellar phase is the L_3 sponge phase that is in equilibrium with almost pure water ($L_3 + W$) in the high temperature region of the phase diagram. The phase diagram as a function of temperature closely resembles the phase diagrams of nonionic microemulsions containing n -alkanes as oil.^{11,12,44,45}

The formation of various phases as a result of phase transitions follows the general trend of decreasing the average mean curvature H of the surfactant monolayer with values being $H > 0$ for the droplet L_1 microemulsion phase, $H = 0$ for the lamellar phase, and $H < 0$ for the L_3 phase. Nonionic surfactants show these general trends, and the observed phase transitions are consistent with a monotonic decrease of the spontaneous

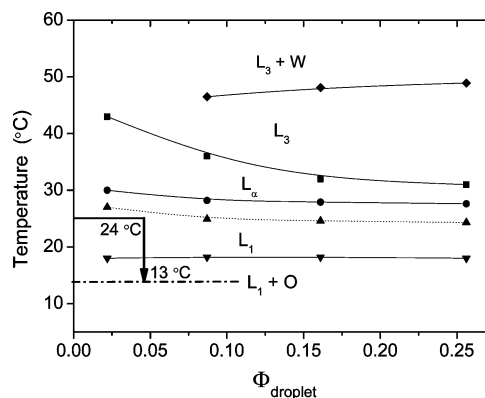


Figure 1. Partial phase diagram of the microemulsion $C_{12}E_5$ /water/1-chlorotetradecane at fixed Φ_s/Φ_o of 0.81 and various droplet concentrations. The arrow indicates the quench region from 24 to 13 °C.

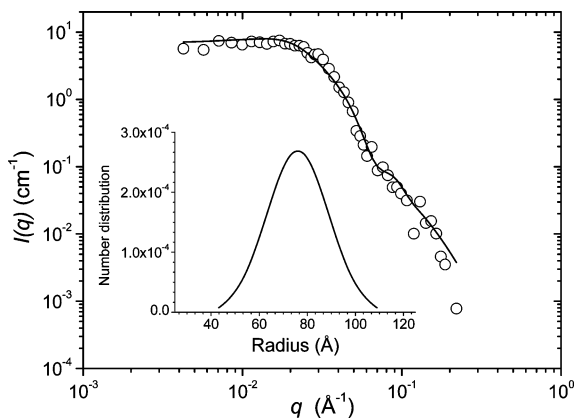


Figure 2. High-resolution SAXS spectra of microemulsion droplets of volume fraction 0.087 and fixed Φ_s/Φ_o ratio of 0.81, measured at 24 °C in the L₁ phase. The solid line is the fit of the polydisperse ellipsoid model described in the text. The inset shows the corresponding size distribution.

mean curvature (H_0) according to the following equation by Helfrich⁴⁶ for the curvature free energy:

$$G_c = \int_{\Sigma} dA [\kappa(H - H_0)^2 + \bar{\kappa}K] \quad (9)$$

where $H = (c_1 + c_2)/2$ and $K = c_1c_2$ are the mean and Gaussian curvatures, respectively, with c_1 and c_2 being the two principal curvatures. With these, the low temperature phase boundary of the microemulsion (L₁) phase can be identified with the emulsification failure boundary as reported by Safran and co-workers⁴⁷ as

$$H_0 > \frac{1}{\rho} \left(1 + \frac{\bar{\kappa}}{\kappa} \right) \quad (10)$$

where ρ is the radius of the stoichiometric sphere which is defined by the ratio Φ_s/Φ_o .

SAXS Measurements in the L₁ Droplet Phase. The SAXS spectra of the microemulsion droplet of volume fraction 0.087 in the L₁ phase at 24 °C are shown in Figure 2 along with the fit. There is good agreement between the fit by the model and the experimental data. Due to the extended q vector from 0.004 to 0.22 Å⁻¹, a well-defined Guinier region is observed. The scattering curve and the fit describe the population of microemulsion droplets alone, without any need for contrast matching. The size distribution of the microemulsion droplets is shown as an inset in Figure 2. The distribution is Gaussian with a radius of 76 Å and an eccentricity of 1.5 (prolate droplets) which is in agreement with the ternary system, C₁₂E₅/water/*n*-decane.^{44,45} Another size distribution of a similar width and shape can also be used to fit the data, and we do not therefore throw any special emphasis on the actual shape.

Temperature Quench and Phase Separation. Perturbation of the microemulsion droplets from equilibrium and the initiation of emulsification failure were achieved as follows. The microemulsion of droplet volume fraction 0.087 was temperature quenched from 24 °C (L₁ droplet phase) to 13 °C in the unstable region (L₁+O). The region of the temperature quench is marked with an arrow in Figure 1. In the unstable region, the L₁ phase coexists with an excess oil phase (L₁+O) and phase separation occurs with excess oil as the second phase. In the microemulsion, Φ_s/Φ_o is fixed at 0.81 and the area per surfactant molecule in the droplet interface is almost constant. Therefore, the geometrical constraint to pack a given volume in a given area thus provides a defined value to the radius of the apolar core (R_c) of the microemulsion droplet as

$$R_c = \frac{3 \left(\frac{\Phi_o}{\Phi_s} + 0.5 \right) V_s}{a_s} \quad (11)$$

where V_s is the volume of the surfactant (C₁₂E₅) molecule and the value of 0.5 arises from the fact that about half the volume of the C₁₂E₅ molecule comes from the hydrocarbon volume. The optimal radius of the droplet matches precisely the spherical radius that is determined by the defined packing constraints, and this happens at the phase boundary of the microemulsion phase which is given by the relation^{44–47}

$$\frac{R}{R_0} = 1 + \frac{\bar{\kappa}}{2\kappa} + \frac{k_B T}{\kappa} f(\phi) \quad (12)$$

where $R_0 = 1/H_0$, κ , and $\bar{\kappa}$ are the spontaneous radius, the bending rigidity constant, and saddle-splay constant, respectively. The last term $[(k_B T/\kappa)f(\phi)]$ in the above equation is the small contribution resulting from the entropy of mixing the droplets in the continuous medium.^{48–50}

Upon quenching the L₁ phase into the unstable region, the spontaneous radius decreases. In order to optimize the curvature free energy, the microemulsion system responds by expelling the oil, resulting in the formation of droplets with new optimal radius ($R_c = R_0$) plus excess oil that appears as the second phase.

The phase separation in the unstable region was followed by time-resolved SAXS, and the evolution of the scattering curve as a function of time is shown in Figure 3. The forward scattering $I(0)$ increases with time, clearly indicating the contribution from the growing oil droplets as a result of phase separation. The spectra were quantitatively analyzed on an absolute scale by using the polydisperse hard-sphere model, with molecular constraints for the microemulsion droplets and polydisperse sphere model for the oil droplets.^{50,51} For a clearer observation, four SAXS spectra at various time intervals are shown in Figure 4 along with the fit of the described model. The fits are in good agreement with the experimental data, showing the validity and applicability of the present model to the microemulsion system under study.

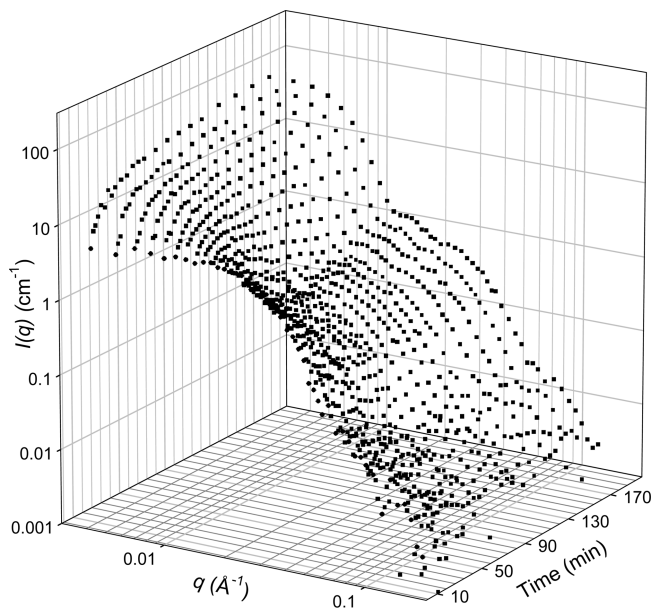


Figure 3. High-resolution SAXS spectra during phase separation in the L₁+O phase at 13 °C, for microemulsion droplet of volume fraction 0.087.

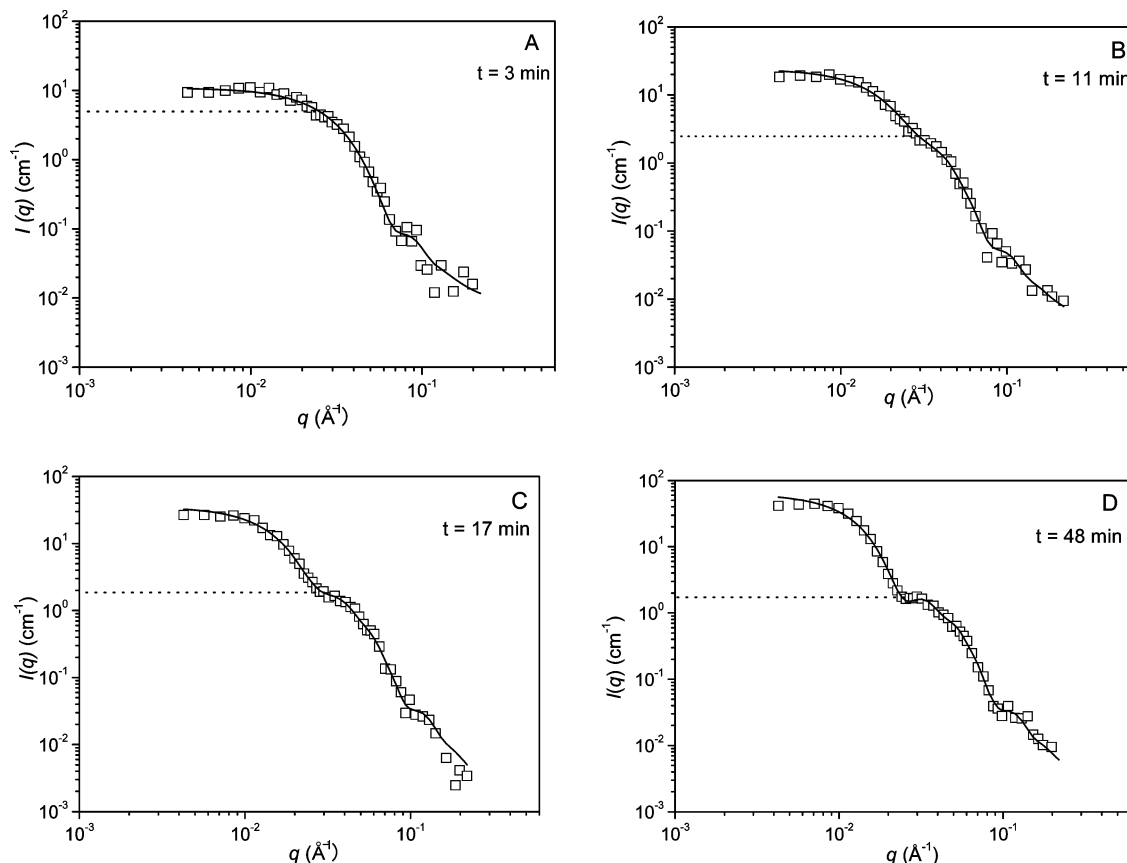


Figure 4. High-resolution SAXS spectra at various times for microemulsion droplet of volume fraction 0.087 in the L_1+O phase at 13 °C. The solid line is the fit of the polydisperse ellipsoid model to the experimental data. (A) 3 min; (B) 11 min; (C) 17 min; (D) 48 min.

At time $t = 0$ (cf. Figure 2), the SAXS spectra describe the presence of a single population of small microemulsion droplets as prolate ellipsoids with a volume equivalent radius of 76 Å and an eccentricity of 1.5. After about 3 min of the quench (Figure 4A), a weak indentation appears at $q = 0.0256 \text{ Å}^{-1}$ marking the decoupling of the superposed scattering intensity curve. This can be identified as the Guinier region of the microemulsion drops. For the first time since the quench, two Guinier regions (apart by a factor of ~ 2) that correspond to oil droplets and microemulsion drops (dotted line in Figure 4A) can be observed. This, together with the increase in the forward scattering intensity of the system, indicates the onset of oil nucleation and the newly formed oil droplets have a radius of 75 Å.

After about 11 min of the quench (Figure 4B), the weak Guinier region of the microemulsion drops gets prominent and moves to higher q (0.028 Å^{-1}) with a decrease in its forward scattering (dotted line in Figure 4B). The forward scattering of the system which is now due to contribution only from the oil droplets shows a significant increase. The presence of two populations in the system can now be clearly observed. With further increase in time ($t = 17$ min), the Guinier region of the microemulsion drops further shifts to large q (0.0298) with further decrease in its forward scattering (dotted line in Figure 4C). The forward scattering from the oil droplets continues to increase as a result of phase separation.

After about 48 min (Figure 4D), the weak indentation that evolved just after 3 min of the quench has become prominent in the q range $0.0254\text{--}0.0321 \text{ Å}^{-1}$. This now corresponds to the secondary maximum in the form factor of a sphere (from the oil droplets). At higher q , one observes features that can be attributed to the equilibrium state of the microemulsion droplets

that corresponds to an equilibrium radius of 51 Å. The presence of two coexisting populations can be clearly observed. Beyond this time (the late stage), the forward scattering intensity of the oil droplets increases and becomes dominant, while the second peak of the form factor (microemulsion drops) remains localized with only smaller changes. Further, the concentration of the evolving large droplets is low and there is no indication of a correlated state, so the distribution is spatially homogeneous. Therefore, the increasing forward scattering intensity of the system can be attributed to the evolution of large oil drops (low concentration) that are dispersed in the system along with small microemulsion droplets. During this fitting procedure, the relative polydispersity (σ_R) was fixed at 0.1350 and an eccentricity of 1.68 was obtained from the fit.

The change in the size of microemulsion droplets and oil droplets as a result of temperature quench is shown in Figure 5. The decreasing size of the microemulsion droplets and the subsequent growth of the oil droplets as time proceeds are clearly observed. The initial process that involves the continuous expulsion of oil from the microemulsion droplets followed by the growth of oil droplets continues up to 48 min when it reaches the steady state. At this time period, all of the expelled oil is present in the large oil drops which then continue to grow by the coarsening process of emulsion systems.

The fraction of oil expelled from the microemulsion droplet during the process of phase separation was obtained from the fit parameter and is shown in Figure 6. The initial oil fraction in the microemulsion droplet decreases steeply and continuously up to the first 45 min after the temperature quench, and beyond which, it remains almost constant. During the expulsion of oil, both surface and volume conservation comes into play through the molecular constraints that are included in the model. The

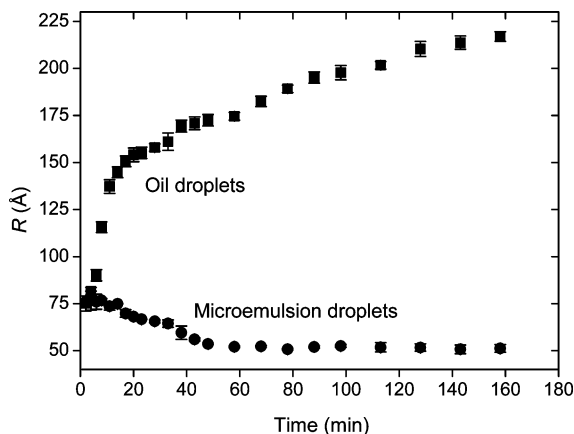


Figure 5. Change in the radius of microemulsion droplets and oil droplets during phase separation.

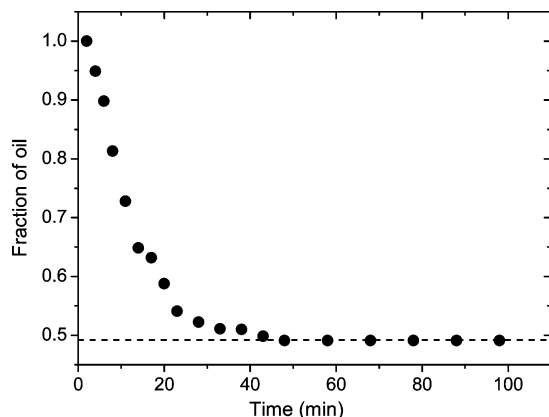


Figure 6. Change in fraction of oil in the microemulsion droplet during phase separation.

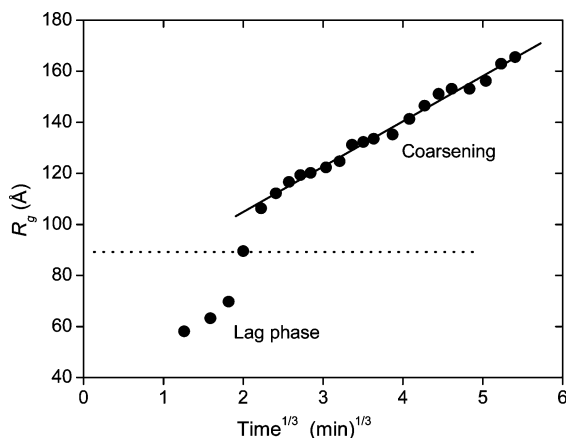


Figure 7. Plot of radius of gyration R_g versus $t^{1/3}$.

initial oil drop fraction in the microemulsion droplet has decreased from 1.00 to 0.49 which is equivalent to the oil droplets containing a fraction of about 0.51 of the total volume of oil. The microemulsion droplets thus retain a fraction of about 0.49 of oil at steady state during the late stage coarsening process.

Figure 7 shows the change in the radius of gyration of the oil drops as a function of $t^{1/3}$. The plot is almost linear, obeying the power law for Ostwald ripening processes ($R_{oil} \propto t^{1/3}$), which is governed by diffusion of single oil molecules in the aqueous phase.^{27,52,53} However, in the immediate vicinity of the quench (up to 9 min), an initial lag phase is observed which can be attributed to the time it takes for the system to react to the

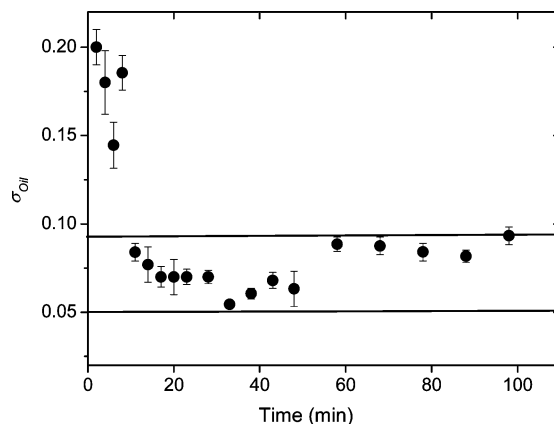


Figure 8. Change of the polydispersity of oil droplets σ_{oil} during phase separation.

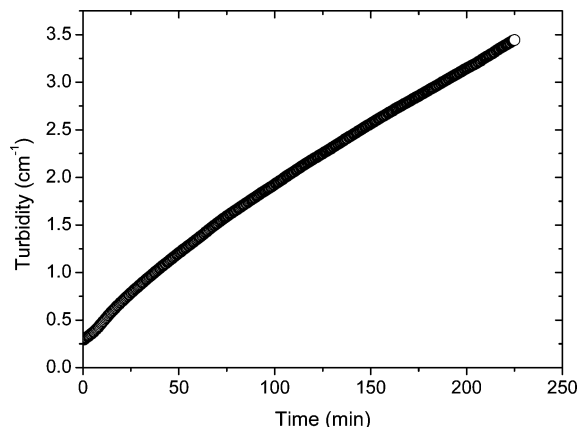


Figure 9. Evolution of turbidity with time at 13 °C for a droplet volume fraction of 0.087 measured at $\lambda = 588$ nm in a quartz cell (Helma) of path length 1 cm.

changes in the surrounding (and hence to optimize the surfactant film curvature) and expel the excess oil from the microemulsion droplets or to the time it takes to nucleate the oil droplets. After this lag period, the oil drops grow almost in a linear manner up to 48 min and thereafter grow by Ostwald ripening at constant volume fraction of oil. By plotting R_g^3 versus time, the rate of ripening was estimated (data not shown). The initial lag phase and the very early stage of emulsification (up to 17 min) have a ripening rate of 0.18×10^{-28} m³/s, indicating nucleation of small oil droplets, while the rate beyond this period is 3.4×10^{-28} m³/s, which indicates a steady coarsening process.

The change in the polydispersity of the oil droplets (σ_{oil}) as a function of time is shown in Figure 8. A drop in polydispersity can be observed during the first 15–18 min due to nucleation processes and thereafter remain constant with small variations. The overall variation for the entire time period is 5–10%. This is considered to be narrow for systems that coarsen in the late stage by an Ostwald ripening mechanism. This, accompanied by an increase in size of the oil droplets, further suggests the mechanism of oil transport in the present microemulsion is mainly by single molecule diffusion.

Turbidity and Radius of Droplets. The time-resolved turbidity (τ) of the microemulsion upon a temperature quench from 24 to 13 °C was also followed. The change in turbidity for a droplet volume fraction 0.087 as a function of time is shown in Figure 9. At $t = 0$, a turbidity of 0.3 cm⁻¹ is observed which is due to the microemulsion droplet population. Also, at short time scale, a weak increase in turbidity is seen which is attributed to the oil nucleation in the lag phase. As time

progresses, the turbidity increases linearly due to the expulsion of oil from the microemulsion droplets. The growing oil droplets then become the dominant scattering particles in the system that contributes to the linear increase in turbidity as time progresses. From the measured turbidity, the size of the growing oil droplets as a function of time was evaluated, which is described in the following section.

Turbidity gives a measure of the reduction in the intensity of light as it passes through a sample (collection of scattering particles) that can scatter light. The fraction of the incident light that is scattered by the sample can conveniently be obtained by integrating the angular scattered intensity function $I(\theta)$ over the surface of a sphere and dividing it by the incident intensity of light I_{inc} as^{17,54}

$$\tau = \frac{1}{I_{\text{inc}}} \int_{\theta=0}^{\pi} \int_{\Phi=0}^{2\pi} I(\theta) x^2 \sin \theta \, d\theta \, d\Phi \quad (13)$$

where θ and x are the scattering angle and the sample-to-detector distance, respectively. When the radius of the scattering particles is much smaller than the wavelength of light ($R \ll \lambda$), the Rayleigh–Gans–Debye (RGD) scattering limit approximation can be used:

$$\frac{I(\theta)x^2}{I_{\text{inc}}} = P(\theta)R_\theta \quad (14)$$

where $P(\theta)$ is the form factor that describes the shape of the scattering particles and R_θ is the Rayleigh ratio. When the radius of the scattering particles is small, $P(\theta)$ can be described by the Guinier approximation as

$$P(\theta) = 1 - \frac{(qR_g)^2}{3} \quad (15)$$

where q is the scattering vector which is defined as

$$q = \frac{4\pi}{\lambda} \sin\left(\frac{\theta}{2}\right) \quad (16)$$

and R_g is the radius of gyration which for a uniform sphere is related to the radius of a sphere R by

$$R_g^2 = \frac{3}{5}R^2 \quad (17)$$

The Rayleigh ratio R_θ is given by

$$R_\theta = K(1 + \cos^2 \theta) \quad (18)$$

where K is defined as the optical constant and is given by the following expression as

$$K = \frac{2\pi^2 n_w^2}{\lambda^4} \left(\frac{dn}{d\Phi}\right)^2 V_{\text{sphere}} \Phi S(0) \quad (19)$$

where n_w , $dn/d\Phi$, V_{sphere} , Φ , and $S(0)$ are the refractive index of water, refractive index increment of the scattering particles, volume of the droplets ($V_{\text{sphere}} = 4\pi R^3/3$), total fraction of scattering particles (we consider only the oil droplets), and structure factor for the limit $q \rightarrow 0$, respectively. We assume the structure factor to be independent in the light scattering q range and contain information concerning particle interactions. For a dispersion of hard spheres, the change in $S(0)$ with the fraction of scattering particles and hence the turbidity is given by the Carnahan and Starling⁵⁵ approximation as

$$S(0) = \frac{(1 - \Phi)^4}{(1 + 2\Phi)^2 - \Phi^3(4 - \Phi)} \quad (20)$$

In the calculation of $dn/d\Phi$, we assume that the scattering is dominated only by the oil droplets that grow as a function of time, and therefore, the contribution of the surfactant was not taken into account. The $dn/d\Phi$ of the oil droplets was evaluated from the following expression⁴⁵ as

$$\frac{dn}{d\Phi} = \frac{3}{2} n_w \left(\frac{n_o^2 - n_w^2}{n_o^2 + 2n_w^2} \right) \quad (21)$$

where n_o and n_w are the refractive index of oil and water, respectively. The refractive indices of oil and water were measured at 13 °C in an Abbey type refractometer operating at a wavelength of 588 nm. The measured values were $n_o = 1.4499$ and $n_w = 1.3340$, and these values were used for the calculations.

Combining the above expressions and substituting in eq 13 leads to

$$\tau = \int_{\theta=0}^{\pi} \int_{\Phi=0}^{2\pi} K(R)(1 - \cos^2 \theta) \times \left(1 - \frac{16\pi^2 R \sin(\theta/2)^2}{5\lambda^2} \right) \sin \theta \, d\theta \, d\Phi \quad (22)$$

Upon expanding the products of eq 22 and integrating, the following expression for turbidity is obtained

$$\tau = \left(\frac{8\pi^3 n_w^2}{3\lambda^4} \left(\frac{dn}{d\Phi}\right)^2 \Phi S(0) \right) R^3 \left(\frac{16}{3}\pi - \frac{128}{15} \frac{R^2 \pi^3}{\lambda^2} \right) \quad (23)$$

This can further be rewritten as follows for simplicity

$$\tau = K_1 R^3 \left(\frac{16}{3}\pi - \frac{128}{15} \frac{R^2 \pi^3}{\lambda^2} \right) \quad (24)$$

where the constant K_1 is given by

$$K_1 = \left(\frac{8\pi^3 n_w^2}{3\lambda^4} \left(\frac{dn}{d\Phi}\right)^2 \Phi S(0) \right) \quad (25)$$

Rearranging the terms in eq 22 to evaluate the radius R leads to a fifth-order equation as given below

$$\left(\frac{128\pi^3}{15\lambda^2} \right) R^5 - \left(\frac{16\pi}{3} \right) R^3 + \left(\frac{1}{K_1} \right) \tau = 0 \quad (26)$$

By having a first guess for the value of the radius R , eq 26 was solved using the Newton–Raphson method⁵⁶ for each value of the turbidity versus time. The radius of oil droplets thus determined (with and without offset subtraction, i.e., the extrapolated $t = 0$ turbidity value, cf. Figure 9) is shown in Figure 10. The radius of the oil droplets obtained from SAXS measurements is also plotted in the same figure for comparison. Overall observation between the plots indicates a fair agreement between the radius of oil droplets evaluated from the turbidity and SAXS methods. No structure factor was included in the SAXS evaluation because q was not too low in comparison with the turbidity method. In the vicinity of the initial state, the radius obtained without the offset subtraction is displaced to higher values. As the offset is a result of scattering by the microemulsion droplets, the measured turbidity is the total turbidity of the system which includes both the microemulsion droplets and oil droplets.

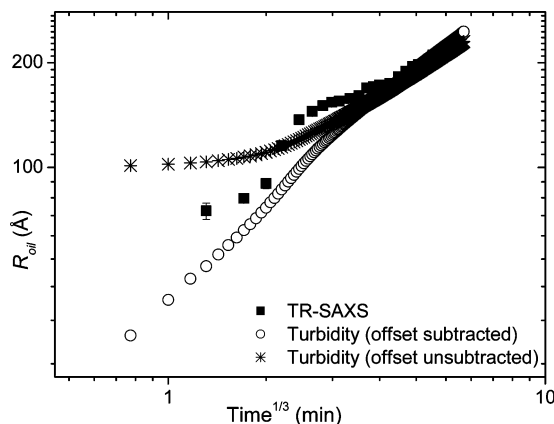


Figure 10. Comparison of the radius of oil droplets evaluated from SAXS and turbidity measurements.

However, after reaching the steady state (~ 48 min), the turbidity is dominated by the oil droplets and the data is in agreement with that obtained by SAXS. The turbidity data with the offset subtraction shows the continuous growth of the oil droplets only, and in addition, the turbidity plots show the existence of a weak lag phase. Further, the two turbidity curves show a linear dependence with the power law of $R_{\text{oil}} \propto t^{1/3}$ indicating that the chief mechanism of material transport upon perturbation in the present microemulsion is by the process of Ostwald ripening.

It is also important to point out that eqs 25 and 26 are valid even in the context of multiple scattering during the turbidity measurements on a UV-vis spectrophotometer. This is because, during such measurements, only the loss in the intensity of light due to scattering by a collection of particles is measured. Worming and co-workers⁵⁷ have clearly shown that under such circumstances multiple scattering effects are small. The main influence of multiple scattering is that it might pollute the direction where the nonscattered light is recorded. Since the measured turbidity is only little influenced by such effects, the size of droplets derived from turbidity experiments will not be influenced by any multiple scattering events.

Conclusions

A new nonionic model microemulsion system consisting of C₁₂E₅/water/1-chlorotetradecane was formulated. The system displayed a temperature-dependent phase behavior exhibiting the various phases, which are also observed in other nonionic ternary systems. Phase separation of the microemulsion was initiated by a temperature quench, and the process was followed by time-resolved laboratory SAXS and time-resolved turbidity methods. Due to the extended range of scattering vector, both small and large drops in the phase separating system are followed without the need of contrasting matching one of the population. Equilibrium of the system is obtained in about 48 min after the temperature quench, and thereafter, the system coarsens at constant oil fraction by the mechanism of Ostwald ripening. The SAXS data was quantitatively studied by fitting the experimental data with polydisperse core-shell ellipsoids of revolution model for the microemulsion droplets and a polydisperse model of spheres for the oil droplets. The growth behavior of the oil droplets at a constant oil fraction and the narrow size distribution of the polydispersity suggest an Ostwald ripening process as the main mechanism of material exchange in this new nonionic microemulsion system containing 1-chlo-

roalkane as oil. The radius of the oil droplets determined by the time-resolved turbidity method agrees with the size evaluated from SAXS and also shows the power law dependence for an Ostwald ripening process. In addition to the demonstration of applying high-resolution time-resolved laboratory SAXS to study the coarsening process in microemulsions, we have further demonstrated that a spectrophotometer with temperature control can be used for size determination of an oil-in-water microemulsion (o/w) on an absolute scale.

Acknowledgment. The authors thank Ulf Olsson, Stefan Egelhaaf, and Carsten Svaneborg for valuable comments and stimulating discussions; Bente Olsen for assistance in the preparation and colloid laboratory; and The Danish Natural Science Research Council (FNU) for financial support.

References and Notes

- (1) Burauer, S.; Sachert, T.; Sottmann, T.; Strey, R. *Phys. Chem. Chem. Phys.* **1999**, 4299.
- (2) Kahlweit, M.; Strey, R.; Busse, G. *J. Phys. Chem.* **1990**, 94, 3881.
- (3) Hellweg, T. *Curr. Opin. Colloid Interface Sci.* **2002**, 7, 50.
- (4) Winsor, A. P. *Solvent Properties of Amphiphilic Compounds*; Butterworth: London, 1954.
- (5) Hamley, I. *Introduction to Soft Matter*; Wiley: Chichester, U.K., 2005.
- (6) Hoar, T. P.; Schulman, J. H. *Nature* **1943**, 152, 102.
- (7) Yagmur, A.; Aserin, A.; Garti, N. *Colloids Surf., A* **2002**, 209, 71.
- (8) Solans, C.; Pons, R.; Kuneida, H. In *Industrial Applications of Microemulsions*; Kuneida, H. Ed.; Marcel Dekker: New York, 1997.
- (9) Paul, B. K.; Moulik, S. P. *Curr. Sci.* **2001**, 80, 990.
- (10) Sjöblom, J.; Lindberg, R.; Fribers, S. E. *Adv. Colloid Interface Sci.* **1996**, 65, 125.
- (11) Olsson, U.; Wennerström, H. *Adv. Colloid Interface Sci.* **1994**, 49, 113.
- (12) Olsson, U.; Nagai, K.; Wennerström, H. *J. Phys. Chem.* **1988**, 92, 6675.
- (13) Kahlweit, M. *Allg. Chem.* **1985**, 97, 655.
- (14) Shinoda, K.; Kuneida, H. *J. Colloid Interface Sci.* **1973**, 42, 381.
- (15) Morris, J.; Olsson, U.; Wennerström, H. *Langmuir* **1997**, 13, 606.
- (16) Strey, R. *Colloid Polym. Sci.* **1994**, 272, 1005.
- (17) Evilevitch, A.; Olsson, U.; Jönsson, B.; Wennerström, H. *Langmuir* **2000**, 16, 8755.
- (18) Taisne, L.; Cabane, B. *Langmuir* **1998**, 14, 4744.
- (19) Shinoda, K.; Arai, H. *J. Phys. Chem.* **1964**, 68, 3485.
- (20) Wadle, A.; Förster, T.; Von Rybinski, *Colloids Surf., A* **1993**, 76, 51.
- (21) Shinoda, K.; Saito, H. *Colloid Interface Sci.* **1968**, 26, 70.
- (22) Ugelstad, J.; Mørk, P. C.; Kaggerud, K. H.; Ellingsen, T.; Berge, A. *Adv. Colloid Interface Sci.* **1980**, 13, 101.
- (23) Pons, R.; Ravey, J. C.; Sauvage, S.; Stébé, M. J.; Erra, P.; Solans, C. *Colloid Surf., A* **1993**, 76, 171.
- (24) Pons, R.; Carrera, I.; Erra, P.; Kuneida, H.; Solans, C. *Colloids Surf., A* **1994**, 91, 259.
- (25) Kabalnov, A. S. *Langmuir* **1994**, 10, 684.
- (26) Binks, B. P.; Clint, J. H.; Fletcher, P. D. I.; Rippon, S.; Lubetkin, S. D.; Mulqueen, P. J. *Langmuir* **1999**, 15, 4495.
- (27) Egelhaaf, S.; Olsson, U.; Schurtenberger, P.; Morris, J.; Wennerström, H. *Phys. Rev. E* **1999**, 60, 5681.
- (28) Vollmer, D.; Strey, R.; Vollmer, J. *J. Chem. Phys.* **1997**, 107, 3627.
- (29) Roshan Deen, G.; Pedersen, J. S. *Z. Metallkd.* **2006**, 97, 3.
- (30) Egger, H.; Sottmann, T.; Strey, R.; Vaero, C.; Berkessel, A. *Tenside, Surfactants, Deterg.* **2002**, 39, 17.
- (31) Arenas, E.; Baran, J. R., Jr.; Pope, G. A.; Wade, W. H.; Weerasooriya, V. *Langmuir* **1996**, 12, 588.
- (32) Baran, J. R., Jr.; Pope, G. A.; Wade, W. H.; Weerasooriya, V.; Yapa, A. *Environ. Sci. Technol.* **1994**, 28, 1361.
- (33) Schwuger, M. J.; Stickdorn, K.; Schomäcker, R. *Chem. Rev.* **1995**, 95, 849.
- (34) Roshan Deen, G.; Pedersen, J. S. *Langmuir* **2008**, 24, 3111.
- (35) Sommer, C.; Roshan Deen, G.; Pedersen, J. S.; Strunz, P.; Garamus, V. M. *Langmuir* **2007**, 23, 6544.
- (36) Maccarini, M.; Briganti, G. *J. Phys. Chem. A* **2000**, 104, 11451.
- (37) Sommer, C.; Pedersen, J. S.; Stein, P. C. *J. Phys. Chem. B* **2004**, 108, 6242.
- (38) Pedersen, J. S. *J. Appl. Crystallogr.* **2004**, 37, 369.
- (39) Fletcher, P. D. I.; Suhling, K. *Langmuir* **1998**, 14, 4065.
- (40) Arleth, L.; Pedersen, J. S. *Phys. Rev. E* **2001**, 63, 61406.

- (41) Pedersen, J. S. *Adv. Colloid Interface Sci.* **1997**, 70, 171.
(42) Vrij, A. *J. Chem. Phys.* **1978**, 69, 1742.
(43) Van Beurten, P.; Vrij, A. *J. Chem. Phys.* **1981**, 74, 2744.
(44) Balogh, J.; Olsson, U.; Pedersen, J. S. *J. Phys. Chem. B* **2007**, 111, 682.
(45) Olsson, U.; Schurtenberger, P. *Langmuir* **1993**, 9, 3389.
(46) Helfrich, B. W. *Naturforsch.* **1973**, 28, 693.
(47) Safran, S. A. *Statistical Thermodynamics of Surfaces, Interfaces and Membranes*; Addison-Wesley: Reading, MA, 1994.
(48) Gradzielski, M.; Langevin, D.; Farago, B. *Phys. Rev. E* **1996**, 53, 3900.
(49) Kegel, W. K.; Reiss, H. *Phys. Chem. Chem. Phys.* **1996**, 100, 300.
(50) Caponetti, E.; Floriano, M. A.; Di Dio, E.; Triolo, E. *J. Appl. Crystallogr.* **1993**, 26, 612.
(51) Reiss, H.; Kegel, W. K.; Groenewold, J. *Phys. Chem. Chem. Phys.* **1996**, 100, 279.
(52) Taylor, P.; Ottewill, R. H. *Colloids Surf., A* **1994**, 88, 303.
(53) Taylor, P. *Adv. Colloid Interface Sci.* **2003**, 106, 261.
(54) Hunter, R. J. *Introduction to Modern Colloid Science*; Oxford University Press Inc: New York, 1993.
(55) Carnahan, W. F.; Starling, K. E. *J. Chem. Phys.* **1969**, 51, 635.
(56) Press, W. H.; Flannery, B. P.; Teukolsky, S. A.; Vetterling, W. T. *Numerical Recipes in Fortran 77*; Cambridge University Press: Cambridge, U.K., 1985.
(57) Worning, P.; Bauer, R.; Øgdenal, L.; Lomholt, S. J. *Colloid Interface Sci.* **1998**, 203, 265.

JP808268M